IEEE Access
Multidisciplinary ⋮ Rapid Review ⋮ Open Access Journal

Received February 12, 2021, accepted February 22, 2021, date of publication February 24, 2021, date of current version March 8, 2021.

Digital Object Identifier 10.1109/ACCESS.2021.3062084

Navigation-Aided Automotive SAR for High-Resolution Imaging of Driving Environments

DARIO TAGLIAFERRI[1], (Member, IEEE), MARCO RIZZI[1], (Graduate Student Member, IEEE), MONICA NICOLI[2], (Member, IEEE), STEFANO TEBALDINI[1], (Senior Member, IEEE), IVAN RUSSO[3], (Senior Member, IEEE), ANDREA VIRGILIO MONTI-GUARNIERI[1], (Senior Member, IEEE), CLAUDIO MARIA PRATI[1], AND UMBERTO SPAGNOLINI[1], (Senior Member, IEEE)

[1]Dipartimento di Elettronica, Informazione e Bioingegneria, Politecnico di Milano, 20133 Milan, Italy
[2]Dipartimento di Ingegneria Gestionale, Politecnico di Milano, 20133 Milan, Italy
[3]Huawei Technologies Italia S.r.l., 20090 Segrate, Italy

Corresponding author: Dario Tagliaferri (dario.tagliaferri@polimi.it)

ABSTRACT The evolution of Advanced Driver Assistance Systems (ADAS) towards the ultimate goal of autonomous driving relies on a conspicuous number of sensors, to perform a wide range of operations, from parking assistance to emergency braking and environment mapping for target recognition/classification. Low-cost Mass-Market Radars (MMRs) are today widely used for object detection at various ranges (up to 250 meters) but they might not be suited for high-precision environment mapping. In this context, vehicular Synthetic Aperture Radar (SAR) is emerging as a promising technique to augment radar imaging capability by exploiting the vehicle motion to provide two-dimensional (2D), or even three-dimensional (3D), images of the surroundings. SAR has a higher resolution compared to standard automotive radars, provided that motion is precisely known. In this regard, one of the most attractive solutions to increase the positioning accuracy is to fuse the information from multiple on-board sensors, such as Global Navigation Satellite System (GNSS), Inertial Measurement Units (IMUs), odometers and steering angle sensors. This paper proposes a multi-sensor fusion technique to support automotive SAR systems, experimentally validating the approach and demonstrating its advantages compared to standard navigation solutions. The results show that multi-sensor-aided SAR images the surrounding with centimeter-level accuracy over typical urban trajectories, confirming its potential for practical applications and leaving room for further improvements.

INDEX TERMS Sensor fusion, automotive SAR, environment mapping, ADAS, in-car navigation, IMU/GNSS integration.

I. INTRODUCTION

Advanced Driver Assistance Systems (ADAS) are electronic devices developed to enable vehicles to assist or even automate some driving functions so as to increase safety and comfort [1]. Examples of ADAS are Adaptive Cruise Control (ACC), where the vehicle supports the driver by automatically adjusting the speed depending on leading vehicle, Lane Change Assistant (LCA), watching for traffic when starting overtaking action, or Cross Traffic Alert (CTA), warning of approaching vehicles at a junction. As driving becomes more automated, ADAS leverage heterogeneous sensors such as cameras, ultrasonic sensors, lidars and radars to perform various operations, from the emergency braking for collision avoidance to the environment perception for object detection and classification [2]. Vehicle-to-Anything (V2X) technologies allow to augment these sensors by enabling cooperative mechanisms [3]. Unlike lidars, low-cost Mass-Market Radars (MMRs) can work at night and in adverse weather conditions, measure radial distance, velocity and angular position of remote targets, the latter feature being enabled by the usage of multiple antennas, i.e., Multiple-Input Multiple-Output (MIMO) radar systems. Nowadays, MMRs operate in the W-band (e.g., 76-81 GHz [4], [5]) and are mostly used for object detection at short, medium or long range (up to 250 meters), due to their limited performance in

The associate editor coordinating the review of this manuscript and approving it for publication was Gerardo Di Martino.

terms of angular resolution - typically > 1 deg -, range, bandwidth and Field of View (FoV), mainly constrained by the currently available integrated circuits technology, number of channels, and sensor cost. The combination of these features limits their performance for high-precision environment mapping in automated driving [4], [6], although some experimental demonstrations of radar-only Simultaneous Localization and Mapping (SLAM) are present in literature [7].

In this context, Synthetic Aperture Radar (SAR) systems are emerging as one of the most promising technologies to perform high-resolution imaging of the driving scenario. Fig. 1 illustrates the list of ADAS-related functionalities along with the enabling sensors, and shows the potential SAR application, complementing lidar and camera sensors for environment mapping and surround view. The envisioned goal is to identify any kind of static and non-static targets such as pedestrians, or other vehicles, with much higher accuracy than existing automotive radars [8]–[11]. The SAR technology employs a moving radar sensor synthesizing a large antenna array by coherently combining different observations in different positions of the trajectory, as sketched in Fig. 2. The range resolution remains the same as for conventional real aperture radars, while the angular resolution increases proportionally to the synthetic aperture, whose size is a function of the carrier wavelength, the minimum vehicle-target distance and the angular sector illuminated by the radar physical beam [12].

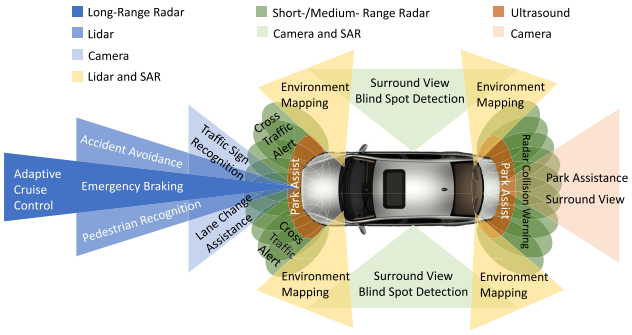

FIGURE 1. Scheme of the sensors used in ADAS. Among the applications, the surrounding environment mapping can be performed using SAR systems.

Nowadays, SAR systems are used for many scientific and military applications, including estimation of hydrological, biophysical, and geophysical parameters on natural scenarios [13], monitoring of sub-wavelength motions of buildings, roads and bridges [14], topographic mapping [15]. The application of SAR techniques to automotive scenarios recently raised the attention of the scientific community. Early works in [8], [9], [16] assess the feasibility of SAR imaging for parking lot detection, by simulations, in-laboratory tests and preliminary outdoor experiments respectively, using a 24 GHz Frequency-Modulated Continuous Waveform (FMCW) radar. These works underline the need of knowing the radar motion along the synthetic aperture

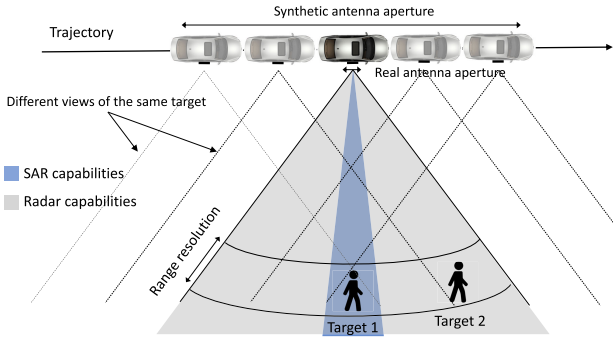

FIGURE 2. SAR working principle: coherent combination of different views of the same target, acquired along an arbitrary but known trajectory (synthetic aperture).

with high precision, analyzing by simulations the effect of a non-straight motion and proposing simple accelerometer- and/or gyroscope-based compensations. Another feasibility study on automotive SAR imaging is in [10], consisting of a side-looking SAR mounted on a linear rail unit, with the aim of imaging two parked cars. In [17], an experimental side-looking SAR system, working at 77 GHz, is mounted on the vehicle's rooftop. The looking direction is set to observe the front-right quadrant of the car, that is at 45 deg from the direction of motion. The results show the practical applicability of automotive SAR imaging to generate meaningful radar images of fences, curbs, parking cars, bushes, and house fronts, at a resolution of 15 cm, using an high-precision (and expensive) Inertial Navigation System (INS), integrating high-precision Inertial Measurement Unit (IMU) (i.e., accelerometers and gyroscopes) and Global Navigation Satellite System (GNSS) data. Further performance investigations are in [18], where a 77 GHz automotive SAR has been mounted on a vehicle travelling on straight paths, and in [19] where a SAR-based parking system is proposed.

An example of sub-THz SAR imaging is provided in [20], [21], where a 300 GHz operating radar with a bandwidth of 40 GHz is mounted on a van, slowly travelling along a linear path, producing high-resolution images of a street and the surrounding objects. In particular, the obtained images show the asphalt structure and even street markings, as well as objects and people on the street. It is highlighted that vital elements for the achievement of these results are again the use of very high-quality IMUs and GNSS sensors, combined with advanced navigation processing to remove any motion error from radar data, so that image focusing is carried out as if the vehicle had travelled along a perfectly known trajectory.

Knowledge about instantaneous radar position and orientation is of paramount importance for automotive SAR systems. Errors in motion estimation (especially along the ranging direction) make the SAR images to appear at different positions, rotated and stretched [22]. An imperfect motion estimate is the result of three factors: *(i)* the degree of unpredictability of the driver's maneuvering (slowly varying term);

(ii) the presence of radar vibrations due to an irregular pavement (fast varying term) and, mostly, *(iii)* the finite accuracy of positioning sensors (e.g., GNSS, IMU, etc.). Traditionally, the residual motion compensation in airborne/spaceborne SAR systems is performed offline from radar and navigation data [23] or even from radar data only, leveraging on fixed targets [24], [25] (*phase calibration methods*). In particular, works in [26], [27] show the 3D imaging of the interior of a Alpine glacier from an aircraft whose flight trajectories were perturbed by strong wind, exhibiting random oscillations of several meters within a single synthetic aperture. One relevant demonstration of the feasibility of SAR imaging from an aircraft forced to fly strongly irregular trajectories is in [28], while authors in [29] demonstrated SAR focusing from circular trajectories. SAR imaging from helicopters and underwater vehicles [30]–[32] are also cases where trajectory is never linear and the platform may slow down or speed up under the action of wind/current (surge).

However, differently from previous works, the main challenge for automotive systems is to operate in real-time (or quasi-real-time), as recently pointed out by [33]–[35], and with cost-effective sensor setups. The estimation of arbitrary vehicle ego-motions from scratch (especially in highly-dynamic scenarios) or from inaccurate navigation data would result in an excessively complex radar-based correction. Similarly, employing high-performance and high-cost navigation systems such as Real Time Kinematics (RTK) or very expensive INS products [36] does not appear practical in automotive scenarios.

In this regard, the most promising approach considers the fusion of multiple sensors to perform high-precision tracking of radar's position and orientation over time [22], [37], [38]. IMU data are typically used to augment GNSS in INS systems [39]–[41]. The fusion of further sensors, available at the ego vehicle, has been shown to improve both the accuracy and the robustness of the positioning system [42]. These can be radars [43], lidars, ultrasonic sensors, camera systems, but also on-board kinematic sensors such as automotive-legacy IMUs, odometer or other vehicle monitoring systems. For the specific automotive SAR application, the most relevant contribution in this sense is [44], where the authors make use of the combination of wheel speeds and acceleration sensors to perform the imaging of a parallel parking bay.

Contributions:

This work focuses on the design and experimental assessment of a multi-sensor navigation algorithm to support automotive SAR imaging for high-resolution mapping of the driving environment. We consider a vehicle equipped with both on-board and dedicated navigation sensors, as portrayed in Fig. 3. We aim to exploit on-board sensors purposely mounted on the vehicle, typically GNSS, IMU, odometer and steering angle (Section IV). Additional high-accuracy dedicated sensors (GNSS and INS) are mounted on radar to be used as benchmarks for navigation assessment. Radar and navigation data are jointly processed by the Vehicle Processing Unit (VPU) to obtain the SAR image. We aim at

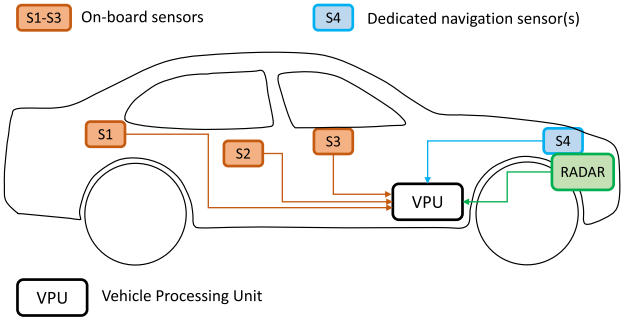

FIGURE 3. Vehicle sensor equipment: on-board (orange boxes) and additional dedicated sensors (blue boxes). Radar and navigation data are jointly processed by the VPU to obtain the SAR image.

investigating, against extensive experimental data, to what extent the fusion of multiple on-board sensors can effectively enable accurate SAR imaging in real driving scenarios. In particular, we are interested in evaluating whether SAR imaging can rely on in-car navigation systems to form a meaningful image, or an additional radar-based motion correction is needed to improve the quality of the environment mapping.

The original contributions of the paper are as follows:

- We propose to support automotive SAR imaging with an ad-hoc navigation system based on a Bayesian tracking filter for fusion of multiple and heterogeneous sensors. In particular, we integrate GNSS, IMUs, wheel-based velocity sensors and a steering angle sensor, by an Unscented Kalman Filter (UKF), for real-time implementation.
- We assess the proposed sensor fusion enabled SAR imaging by exploiting experimental data collected in a dedicated acquisition campaign. Tests have been conducted using a purposely re-adapted, fully equipped commercial vehicle driving with moderate-to-low speed (up to 25 km/h, limited by radar equipment) over non-straight trajectories in urban environments. SAR images are obtained with the well-known Time Domain Back-Projection (TDBP) focusing algorithm, which is standard for high-quality SAR imaging in remote sensing applications whenever the assumptions of straight trajectory and constant speed cannot be retained, as here [27], [28], [45]. The results demonstrate that the proposed multi-sensor tracking technique definitively improves the quality of the SAR images, evaluated by means of reference targets of known shape and dimensions, compared to standard navigation solutions. We show how the accuracy of a commercial automotive-legacy IMU+GNSS platform, rigidly mounted on the radar's equipment thus providing a proprietary INS solution, is not enough in detecting sub-meter vehicle motions, leading to defocused SAR images. Conversely, the integration of on-board sensors by the proposed navigation filter enables the SAR imaging system to map the surrounding environment with a

centimeter-level accuracy, without any additional phase calibration method.
- We show that, on the non-straight trajectories used for testing, the proposed SAR ad-hoc navigation method from on-board sensors attains the same performance of a further, ad-hoc processing of IMU and GNSS data from the dedicated on-radar IMU+GNSS platform. This result suggests that, for typical urban routes, there is no need of additional automotive-compliant sensors to operate SAR systems, but it is enough to exploit in-car sensors, provided that and ad-hoc processing unit is used for data fusion and imaging. Even if numerous open challenges remain open, we are now able to identify a set of future research directions.

Organization:

The paper is organized as follows: Section II describes the navigation algorithms employed in this work; Section III details the SAR signal processing method; Section IV describes the experimental data acquisition campaign; Section V reports the results of SAR imaging while Section VI draws the conclusions and discusses the open challenges.

Notation: Bold upper- and lower-case letters describe matrices and column vectors. The complex conjugate of a scalar/vector/matrix is indicated with $(\cdot)^*$. Matrix transposition is indicated as $(\cdot)^{\mathrm{T}}$. $\mathbf{1}_N$ denotes a column with all entries equal to 1. $\mathbb{R}$ is the symbol for the set of real numbers. Operator $\|\cdot\|_2$ represents the Euclidean norm.

II. RADAR NAVIGATION

Section I outlined the need for high-precision tracking of the position and orientation of the radar equipment. In is important to point out that, for automotive SAR, this requirement is not on absolute positioning over the whole vehicle trajectory, but rather on the *relative* radar's motion over the synthetic aperture distance (up to 1 m in this work). To perform such a tracking, three reference systems are needed, as illustrated in Fig. 4. The first one, referred as navigation reference system (superscript n), is fixed with respect to the Earth and centered in a suitable geographic point to describe the radar motion. The second reference system is vehicle-fixed with axes originated from the vehicle Center of Gravity (CoG), and it is usually referred to as body reference system (superscript b). Finally, the third reference system is radar-fixed, centered and aligned with the radar antenna. In this section, we focus on tracking the position, velocity and orientation of the b-system (vehicle) with respect to the n-system, assuming that the radar sensor is *rigidly* mounted on the vehicle, i.e., its position and orientation can be retrieved from the vehicle one with a known (fixed) roto-translation, that depends on the radar mounting position from vehicle's CoG. In this setting, experimentally verified in Section V, vehicle tracking (navigation) is practically equivalent to the tracking of the radar equipment.

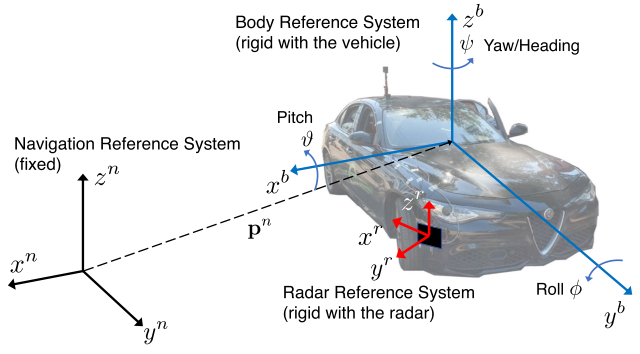

FIGURE 4. Reference systems used for tracking the radar equipment, with the vehicle position in the *n*-system and the rotation angles of the *b*-system with respect to *n*-system.

Based on the above assumption, the instantaneous 3D position of the vehicle can be expressed in the n-system as:

$$\mathbf{p}^n = \left[p_x^n \; p_y^n \; p_z^n\right]^{\mathrm{T}} \in \mathbb{R}^{3\times 1}. \tag{1}$$

Vehicle orientation can be described by the Euler angles, i.e., the rotation angles of the b-system around x^n, y^n and z^n axes, which are called pitch, roll and yaw/heading, respectively [41]:

$$\boldsymbol{\eta}^b = [\vartheta \;\; \phi \;\; \psi]^{\mathrm{T}}. \tag{2}$$

For tracking applications, it is convenient to represent these angles by the equivalent unit quaternions [40]:

$$\mathbf{q}^b = [q_0 \; q_1 \; q_2 \; q_3]^{\mathrm{T}} \in \mathbb{R}^{4\times 1}, \quad \left\|\mathbf{q}^b\right\|_2 = 1, \tag{3}$$

which generalizes the concept of complex numbers to describe a 3D rotation of the b-system with respect to the n-system.

In the following, we first describe the conventional approach for navigation by IMU+GNSS integration, then we propose an ad-hoc method which fuses further available sensors to optimize the navigation performance for the SAR imaging purpose. The first approach is standard in commercial INS devices, for 3D navigation applications (e.g., Unmanned Aerial Vehicles (UAV), cars, etc.), while the second is suited to a multi-sensor integration scenario, where the vehicle travels over planar trajectories and the SAR imaging is 2D.

A. IMU+GNSS INTEGRATED NAVIGATION

As conventional approach for in-car navigation, we consider the fusion of IMU and GNSS data by a Bayesian filter, that tracks the 3D position $\mathbf{p}_k^n$, the 3D velocity $\mathbf{v}_k^n = [v_{x,k}, v_{y,k}, v_{z,k}]^{\mathrm{T}}$ and the orientation $\mathbf{q}_k^b$ of the vehicle at time $t = kT$, with T the sampling time of the sensors. To simplify the notation, we drop the superscripts (n and b) indicating the reference system, and we denote the vehicle state to be tracked as:

$$\boldsymbol{\theta}_k = \left[\mathbf{p}_k^{\mathrm{T}} \; \mathbf{v}_k^{\mathrm{T}} \; \mathbf{q}_k^{\mathrm{T}}\right]^{\mathrm{T}} \in \mathbb{R}^{10\times 1}. \tag{4}$$

The state transition from time $k-1$ to time k is modelled by a non-linear function $\mathbf{f}(\cdot)$, that describes the evolution from the

state $\boldsymbol{\theta}_{k-1}$ to the next one $\boldsymbol{\theta}_k$, as the result of a set of control inputs $\mathbf{u}_{k-1}$ and a process noise $\mathbf{w}_k$:

$$\boldsymbol{\theta}_{k|k-1} = \mathbf{f}\left(\boldsymbol{\theta}_{k-1}, \mathbf{u}_{k-1}, \mathbf{w}_k\right), \tag{5}$$

in which $\mathbf{w}_k \sim \mathcal{N}(\mathbf{0}, \mathbf{C}_{w,k})$ is zero mean, Gaussian-distributed with a time-varying covariance matrix $\mathbf{C}_{w,k}$. The control input $\mathbf{u}_{k-1}$, for the specific problem at hand, consists in the 3D acceleration and 3D angular velocity measured by the IMU in its local reference system, here assumed to be aligned with the the b-system, that is affected by slowly time-varying biases and noise. By using IMU measurements as input to the state evolution, the change in position, velocity and orientation is directly modeled in terms of the inertial measurements. The term $\mathbf{w}_k$ accounts for the IMU measurement noise (see [40] for further details). Notice that the IMU bias is one of the most detrimental parameters affecting the performance of a tracking filter. For both accelerometers and gyroscopes, the bias can be split into a constant component, varying from run to run (turn-on bias), and a time-varying component, varying over periods of order a minute (bias instability). Typically, automotive-legacy IMUs (of cost $50 - 500$ \$) are characterized by a turn-on bias > 0.1 m/s^2 and a bias stability > 0.01 m/s^2 for accelerometers and by $> 25 \times 10^{-3}$ deg/s and $> 5 \times 10^{-4}$ deg/s, respectively, for gyroscopes [41]. For reference comparison, for an aviation-legacy IMU (with cost in the order of 100000 \$), the previous values can be three or four orders of magnitude less. A thorough review of IMU parameters and performance in navigation can be found in [41], [46]–[48].

The navigation state $\boldsymbol{\theta}_k$ is embedded in a set of noisy observations:

$$\mathbf{z}_k = \mathbf{h}\left(\boldsymbol{\theta}_k, \mathbf{n}_k\right), \tag{6}$$

where $\mathbf{h}(\cdot)$ is a generic non-linear function and $\mathbf{n}_k$ denotes the measurement noise, modelled as zero-mean, Gaussian-distributed with time-varying covariance matrix $\mathbf{C}_{n,k}$. The set of observations comprises the measurements of 3D position, 3D velocity and heading from GNSS, here modelled as, respectively:

$$\begin{aligned} \mathbf{z}_{p,k}^{\text{gnss}} &= \mathbf{p}_k + \mathbf{n}_{p,k}^{\text{gnss}}, \\ \mathbf{z}_{v,k}^{\text{gnss}} &= \mathbf{v}_k + \mathbf{n}_{v,k}^{\text{gnss}}, \\ z_{\psi,k}^{\text{gnss}} &= \psi_k + n_{\psi,k}^{\text{gnss}}. \end{aligned} \tag{7}$$

where $\mathbf{n}_k = [\mathbf{n}_{p,k}^{\text{gnss,T}}, \mathbf{n}_{v,k}^{\text{gnss,T}}, n_{\psi,k}^{\text{gnss}}]^{\text{T}}$. Notice that the covariance of the observation noise, $\mathbf{C}_{n,k}$, is typically time-varying as the GNSS accuracy varies according to the movement and the specific scenario (e.g., urban vs. rural areas).

B. SAR AD-HOC MULTI-SENSOR INTEGRATED NAVIGATION (SAR-MIN)

To improve the navigation performance in SAR application, since the vehicle/radar motion is constrained to a planar trajectory and the SAR focusing is 2D (i.e., along the range and cross-range dimensions), we reduce the tracking to the 2D domain. In addition, we take advantage of the availability of multiple heterogeneous sensors, that are typically integrated in the car. We thus propose to track the 2D vehicle position $\mathbf{p}_k = \left[p_{x,k}\ p_{y,k}\right]^{\text{T}} \in \mathbb{R}^{2\times 1}$, the planar velocity v_k, the heading ψ_k and the heading rate ω_k, represented by the modified state:

$$\boldsymbol{\theta}_k = \left[\mathbf{p}_k^{\text{T}}\ v_k\ \psi_k\ \omega_k\right]^{\text{T}}. \tag{8}$$

The state evolution is here chosen to follow the Constant Turn Rate and Velocity (CTRV) model [49] to best represent the dynamics experienced in the experimental campaign (Section IV), characterized by slowly-changing velocities and moderate heading rates.

As concerns the set of observations, we consider to integrate the GNSS measurements, $N > 1$ on-board IMUs (given the problem at hand, only gyroscopes are considered), four wheel-based velocity sensors and the wheels' steering angle sensor:

$$\begin{aligned} \mathbf{z}_{p,k}^{\text{gnss}} &= \mathbf{p}_k + \mathbf{n}_{p,k}^{\text{gnss}}, \\ z_{v,k}^{\text{gnss}} &= v_k + n_{v,k}^{\text{gnss}}, \\ z_{\psi,k}^{\text{gnss}} &= \psi_k + n_{\psi,k}^{\text{gnss}}, \\ \mathbf{z}_{\omega,k}^{\text{gyro}} &= \omega_k \mathbf{1}_N + \mathbf{b}_{\omega,k} + \mathbf{n}_{\omega,k}^{\text{gyro}}, \\ \mathbf{z}_{v,k}^{\text{wheel}} &= v_k \mathbf{1}_4 + \mathbf{n}_{v,k}^{\text{wheel}}, \\ z_{\gamma,k}^{\text{steer}} &= \tan^{-1}\left(L_y \frac{\omega_k}{v_k}\right) + n_{\gamma,k}^{\text{steer}}, \quad v_k \neq 0 \end{aligned} \tag{9}$$

where we assume the N gyroscopes (e.g., $N = 3$ in Section IV) to be all equally oriented with the vehicle (b-system) and we indicate with $\mathbf{b}_{\omega,k} \in \mathbb{R}^{N\times 1}$ their slowly time-varying biases. In (9), L_y denotes the wheelbase, i.e., the distance between the centers of the frontal and rear wheels. Notice that the model for the steering angle sensor applies only for non-null (or non-negligible) velocities [50].

Bayesian tracking of vehicle/radar dynamics based on multiple in-car sensor integration is implemented using an UKF filter [51] applied to the dynamics and measurement models above introduced; implementation details are omitted as they can be derived from the mentioned models.

As it will be shown in Section V, the proposed approach allows to obtain a much less sensitive tracking with respect to IMU biases compared to standard IMU+GNSS solutions. The result is an overall smoother trajectory, that largely improves SAR focusing.

III. RADAR SIGNAL PROCESSING

MMRs can be classified according to the application as [4]: *(i)* long-range radars, for narrow-beam forward looking applications (e.g., ACC); *(ii)* medium-range radars, mostly for CTA; *(iii)* short-range radars for proximity sensing, as obstacle detection and parking aid (see Fig. 1). Each of these categories has some features limiting the application to environmental mapping, mostly related to the low angular resolution (> 1 deg), which is ruled by the real aperture of the MIMO radar, or to the short range/moderate bandwidth [4].

Although high-performance High-End Radars (HERs) were designed to overcome MMRs limitations, their costs is prohibitive for mounting on private cars [6]. This section briefly reviews the signal processing of standard automotive MIMO radars (MMR and HER), and then presents the proposed approach for SAR imaging, highlighting the advantages over conventional radar imaging.

A. AUTOMOTIVE RADAR SIGNAL PROCESSING

The typical automotive radar is a FMCW system transmitting a modulated chirp signal in W-band (76 - 81 GHz) [52]. During the chirp duration, T_p, the carrier frequency is linearly increased from the starting frequency f_0, up to $f_0 + B$, where B is the radio-frequency bandwidth. The transmitted signal, repeated every Pulse Repetition Interval (PRI), is therefore:

$$s(t) = \cos(2\pi f_0 t + \pi K t^2) \tag{10}$$

where $K = B/T_p$ is the chirp rate and t is commonly referred to as *fast-time*. The dechirp-on-receive operation mixes the transmitted signal $s(t)$ with the received signal, a delayed and attenuated version of $s(t)$, to generate the beat signal. Neglecting high-frequency components, filtered out before digitalization, the beat signal is:

$$\begin{aligned} s_B(t; T_D) &= \alpha\, s(t - T_D)\, s(t) \\ &= \alpha\, \cos(2\pi f_0 T_D + 2\pi K T_D t - \pi K T_D^2), \end{aligned} \tag{11}$$

where α comprises the path-loss and the scattering of the target, and the frequency of the beat signal is function of the two-way propagation delay between sensor and target:

$$T_D = \frac{2R}{c}, \tag{12}$$

where $c = 3 \times 10^8$ m/s and R is the distance between of target from the sensor. The last phase term in (11) is the so-called residual video phase, peculiar of FMCW architectures. As this term depends on the delay squared, it is generally negligible for short-range radars.

The matrix of radar's raw data refers to the beat signals, function of the fast-time t, associated to the superposition of all the target echoes collected at each PRI, known as *slow-time* τ:

$$d_{RAW}(t, \tau) = \sum_{\ell} s_B(t; T_D^{(\ell)}(\tau)) \tag{13}$$

where the index ℓ refers the ℓ-th target. Notice that the two-way delay T_D is function of the slow-time τ.

The first processing step for a standard FMCW radar is the Range-Compression (RC) of the raw data $d_{RAW}(t, \tau)$, consisting of a proper filtering to produce a sharp peak in correspondence of the signal delay. RC data are obtained through: (*i*) a Fourier transform along the fast-time t dimension of the raw data $d_{RAW}(t, \tau)$; (*ii*) a scaling factor on the the beat frequency f, i.e., $f = Kt$ and (*iii*) the removal of the residual video phase by a phase rotation with $\exp(+j2\pi K t^2)$. For a single echo $s_B(t; T_D)$ in (11), the RC signal is thus equal to [52]:

$$\begin{aligned} s_{RC}(t; T_D) &= S_B(f; T_D)\big|_{f=Kt} \exp(+j2\pi K t^2) \\ &= \alpha\, T_p\, \mathrm{sinc}\,[B(t - T_D)] \exp(j2\pi f_0 T_D) \end{aligned} \tag{14}$$

where $S_B(f; T_D)$ is the Fourier transform of $s_B(t; T_D)$ and $\mathrm{sinc}\,[x] = \sin(x)/x$. For the superposition of echoes (13), RC data matrix is therefore:

$$d_{RC}(t; \tau) = \sum_{\ell} s_{RC}(t; T_D^{(\ell)}(\tau)). \tag{15}$$

From (14) it follows that the range resolution ρ_R for a standard automotive radar is dictated by the width of the main lobe of the sinc function, approximated as:

$$\rho_R \approx \frac{c}{2B} \quad [\mathrm{m}], \tag{16}$$

where the factor 2 accounts for the two-way propagation of the signal. Considering a W-band radar with 3 GHz bandwidth, as the one used here in the experimental campaign in Section IV, $\rho_R \approx 5$ cm. The angular resolution is set by the physical antenna aperture, A:

$$\rho_\psi \approx \frac{\lambda_0}{2A} \quad [\mathrm{rad}], \tag{17}$$

where λ_0 denotes the carrier wavelength.

In MIMO radar systems, the angular resolution is achieved by processing the echoes generated by a single transmitter and collected by an array of receivers. This is commonly referred as *multi-channel* processing, where each Tx-Rx pair constitutes a single channel. For a linear, half-wavelength-spaced MIMO radar, (17) depends on the number of antennas N. For instance, an array of $N = 64$ elements, with $\lambda_0/2$ uniform spacing ($A = N\lambda_0/2$), the achievable resolution is approximately 0.9 deg.

B. SAR PROCESSING: TIME DOMAIN BACK-PROJECTION

The goal of the automotive SAR imaging presented herein is to resolve the 2D (or possibly 3D) positions of targets with finer accuracy compared to standard MIMO radars. The core is the focusing stage, which aims at coherently processing echoes collected at different positions along the vehicle trajectory. SAR resolves targets in the cross-range dimension and translate data from fast- slow-time domains to a Cartesian reference system.

The strongly non-straight nature of typical automotive trajectories calls for a TDBP-based focusing algorithm, which yields an exact reconstruction of the observed space, given the *precise* knowledge of the vehicle motion along the synthetic aperture, at the price of being computationally expensive [45]. For a single-antenna radar, the 2D imaging by TDBP consists of a 2D correlation between the radar data $d_{RC}(t; \tau)$ with the expected 2D response of a theoretical target from each coordinate pair (x, y) (pixel) in the sensed region of the image (Fig. 5):

$$I(x, y) = \iint d_{RC}(t; \tau)\, s_{RC}^*(t; T_D(\tau; x, y))\, \mathrm{d}t\, \mathrm{d}\tau, \tag{18}$$

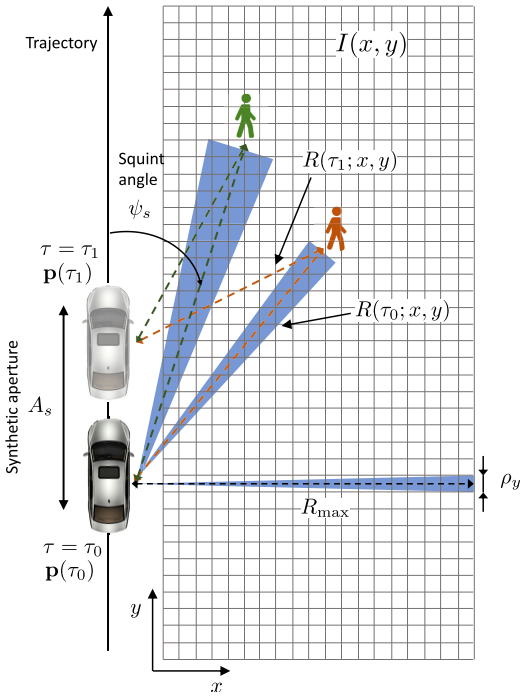

FIGURE 5. Sketch of the quantities involved in the TDBP integral computation.

where $T_D(\tau; x, y)$ is the two-way propagation delay between any given point of the radar trajectory at time τ and the 2D grid coordinates (x, y). Its expression is:

$$T_D(\tau; x, y) = \frac{2R(\tau; x, y)}{c} = \frac{2}{c}\sqrt{(x - p_x(\tau))^2 + (y - p_y(\tau))^2 + (h - p_z(\tau))^2} \tag{19}$$

where $p_x(\tau)$, $p_y(\tau)$ and $p_z(\tau)$ denote the radar antenna coordinates at discrete time τ, obtained from the tracking filter, and h represents the height of the focusing plane from ground. From (14) and (18), it is straightforward to observe that the TDBP is composed by three steps: (1) an interpolation of the RC data along the fast-time axis t by means of the sinc function in (14); (2) a phase rotation to the carrier frequency f_0 by means of $\exp(-j2\pi f_0 T_D)$; (3) a summation over the slow-time axis τ (i.e., along the synthetic aperture).

Eq. (18) can be extended to the general MIMO case to form the multi-channel image, as *coherent* sum of the images $I^{(ch)}(x, y)$ obtained from each Tx-Rx pair:

$$I(x, y) = \sum_{ch} I^{(ch)}(x, y). \tag{20}$$

While the range resolution remains the same of real aperture radars (Subsection III-A), the angular resolution of a SAR system is obtained as the resolution of an ideal equivalent array of length equal to the processed synthetic aperture A_s, as

$$\rho_\psi^{\text{SAR}} \approx \frac{\lambda_0}{2A_s \sin(\psi_s)} \quad [\text{rad}], \tag{21}$$

where ψ_s is the so-called squint angle with respect to the radar direction of motion (i.e., vehicle motion) such that $\psi_s = 0$ deg along the track (Fig. 5). The resolution of the SAR system is maximum for $\psi_s = 90$ deg and degrades as $\psi_s \to 0$ for a fixed synthetic aperture A_s. The corresponding linear resolution in the direction of motion at a given maximum range $R_{\max}$ is

$$\rho_y \approx \rho_\psi^{\text{SAR}} \cdot R_{\max} \quad [\text{m}]. \tag{22}$$

The synthetic aperture length A_s is usually chosen as a trade-off between the desired resolution at a given maximum range and the computational burden. For example, for a system operating around 77 GHz, a linear resolution in the direction orthogonal to sensor trajectory of 5 cm for a target 50 m away from the radar is obtained with a synthetic aperture length of around 2 m. The resolution gain compared to a real aperture radar, whose size at 77 GHz is limited to one-to-few cm, is evident. Table 1 summarizes the performance of current MMRs, HERs and SAR systems for automotive applications. SAR systems do not necessarily need to employ a huge number of antennas, allowing the use of low-cost devices, at the price of a more sophisticated processing.

It is worth observing that, in principle, a relative range error of $\lambda_0/4$ within the synthetic aperture A_s (e.g., due to inaccurate motion estimation) is enough to negatively affect the focusing in (18). In automotive SAR applications, with the radar working in W-band, the previous considerations would theoretically push for a mm-scale accuracy in navigation within the aperture A_s, to track both macro-scale and micro-scale motions (e.g., vibrations), which cannot be achieved with typical automotive sensors and real-time approaches. However, Section V demonstrates the feasibility of automotive SAR imaging in typical urban scenarios with an affordable, cm-accurate navigation.

C. STRIPMAP SAR PROCESSING

For W-band MIMO radars, the size of the antennas is compact and thus it implies a wide FoV, i.e., physical beam. This means that, for each radar's position along the trajectory, the TDBP integral (18) must be computed on a huge number of points of the Cartesian grid, leading to an unbearably computational burden for automotive scenarios. To address this issue, we propose to limit the computation (18) to a sub-set of angles of arrival, ψ, enforced with a spatial filter $W(\psi(\tau; x, y))$, reducing the radar's FoV. The method, whose principle of operation is sketched in Fig. 6, is commonly referred to as *stripmap SAR processing* [53], and the TDBP integral (18) becomes:

$$I(x, y) = \iint W(\psi(\tau; x, y)) \times d_{RC}(t, \tau)\, s^*_{RC}(t; T_D(\tau; x, y))\, \mathrm{d}t\, \mathrm{d}\tau. \tag{23}$$

If, on one side, the computational complexity of the method is strongly reduced, narrowing the radar FoV, and thus the processed beam, implies that each target can be illuminated only along a shorter synthetic aperture, A_s^{strip}, and the

TABLE 1. Performance parameters of current MMRs, HERs and SAR systems for automotive.

		Long-range MMR	Medium-range MMR	Short-range MMR	HER	SAR
Carrier frequency f_0	[GHz]	76-77	77-81	77-81	77-81	76-81
Bandwidth B	[GHz]	≤ 0.6	≤ 0.6	≤ 4	≤ 4	≤ 4
Maximum range $R_{\max}$	[m]	250	100	30	250	250
Range resolution ρ_R	[cm]	25	25	5	5	5
FoV (azimuth) Ω	[deg]	$\pm$ 15,	$\pm$ 40	$\pm$ 80	$\pm$ 60	$\pm$ 80
Aperture	-	real	real	real	real	synthetic
Angular resolution (azimuth) ρ_ψ	[deg]	≈ 1	> 1	$\gg 1$	≈ 1	arbitrary (< 1)

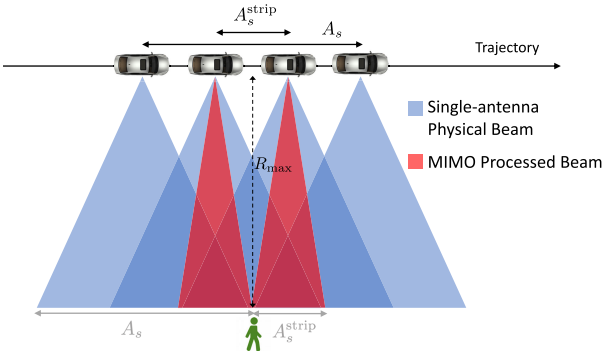

FIGURE 6. Stripmap SAR: by limiting the processed beam to a portion of the physical one, the compuational burden associated to TDBP is strongly alleviated at the expense of a reduction in angular resolution by a factor A_s^{strip}/A_s.

angular/linear resolution decreases accordingly by a factor A_s/A_s^{strip}. A thorough discussion on the computational burden of SAR focusing algorithms and their comparison goes beyond the scope of the paper, but some guidelines and possibilities are reported in Section VI.

D. PULSE REPETITION FREQUENCY AND MAXIMUM VELOCITY CONSTRAINT

In addition to the computational complexity of TDBP, one of the challenging aspects in SAR system design is represented by the trade-off between vehicle velocity v and Pulse Repetition Frequency (PRF). Indeed, PRF should be high enough to ensure a sufficiently dense and uniform sampling of the synthetic aperture, to prevent the arising of imaging artefacts due to ambiguities (*ghost targets*). Formally, the condition required to achieve correct imaging is, for a single-antenna radar [12]:

$$\text{PRF} \geq \frac{4}{\lambda_0} v \sin\left(\frac{\Omega}{2}\right) \approx \frac{4}{\lambda_0} v \tag{24}$$

where $\lambda_0/4$ is the required spatial sampling along the aperture, Ω is the beamwidth of the radar antenna and the approximation (24) is for very wide beamwidths (isotropic antennas). The constraint in (24) strongly limits the application to high-mobility scenarios, as a PRF of 1 kHz ($f_0 = 77$ GHz) would allow for a maximum speed of $v_{\max} = \text{PRF}\lambda_0/4 \approx 1$ m/s. The limitation by (24) can be relaxed by the use of MIMO radars. The higher directivity achieved by using multiple antennas ensures the rejection of all the ambiguities outside the MIMO radar FoV. These normally arise in single-channel radars due to insufficient spatial sampling of the synthetic aperture, or equivalently, higher vehicle speeds. In general, for a given PRF, the velocity upper limit $v_{\max}$ scales approximately with the number of radar channels, N, for unambiguous SAR imaging [31], [54].

TABLE 2. ScanBrick® parameters configuration.

Parameter	Symbol	Value(s)
Carrier frequency	f_0	77 GHz
Bandwidth	B	3 GHz
Active Tx Channels	N_{Tx}	3
Active Rx Channels	N_{Rx}	4
Pulse Repetition Frequency	PRF	990 Hz
Maximum range	$R_{\max}$	27 m
Single-antenna beamwidth	Ω	120 deg

IV. DATA ACQUISITION CAMPAIGN

To validate the proposed solution for high-precision in-car navigation and SAR imaging, we carried out a number of experiments with a fully equipped vehicle. The vehicle is an over-sensorized Alfa Romeo Giulia "veloce" car portrayed in Fig. 7 with the skecth of the sensor equipment. The SAR capabilities are enabled by a proprietary ScanBrick® W43 platform from ARESYS S.r.l., a FMCW quasi-monostatic 3 × 4 MIMO radar with integrated patch antennas, operating in W-band (3 GHz bandwidth), equipped with up to 4 simultaneous receiving channels and up to 3 active transmitting channels. The system is based on standard automotive technologies suitable for future mass market applications, both from performance and price point of view. In particular, the Radio Frequency module is based on Texas Instrument AWR1243 board, while the base-band module is designed by ARESYS S.r.l. The ScanBrick® configuration used for the acquisition campaign is summarized in Table 2. The radar case is rigidly mounted in the front bumper of the vehicle, resulting in a radar bore-sight at a squint angle of 45 deg with respect to the direction of motion, about 0.5 m above ground. The ScanBrick® is powered by a standard car battery placed inside the front storage compartment of the car. Each acquisition is logged with a laptop and UTC time-synchronized.

The car equipment is complemented by both on-board and dedicated (mounted for the experiments) navigation sensors,

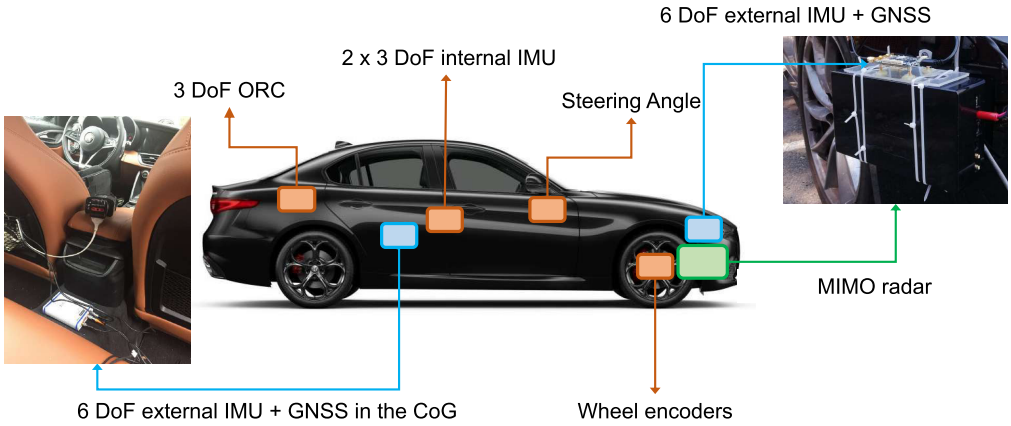

FIGURE 7. Alfa Romeo Giulia "veloce" car re-equipped for the experimental data acquisition campaign. With reference to Fig. 3, orange boxes indicate on-board sensors, blue boxes additional navigation sensors (one in the CoG and the other placed on top of the radar, represented by a green box).

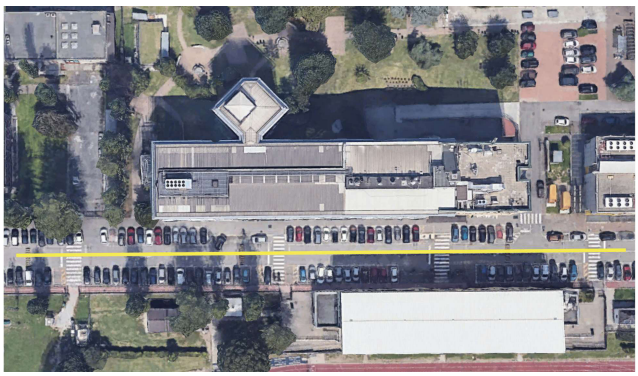

(a)

FIGURE 8. Satellite view of the experimental campaign scenario: closed road (highlighted in yellow) in front of the Dipartimento di Elettronica, Informazione e Bioingegneria Politecnico di Milano.

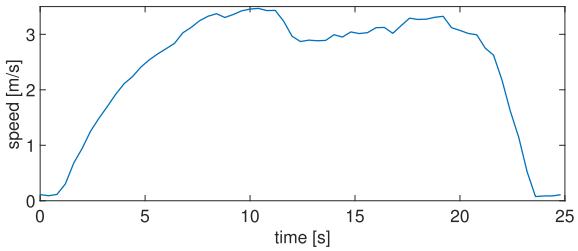

FIGURE 9. GNSS-estimated vehicle speed in Test 1.

as anticipated in the introduction. The on-board equipment comprises:

- two 3 Degrees of Freedom (DoF) IMUs, measuring lateral and longitudinal acceleration, along with heading rate. The locally acquired measurements are available with 500 Hz sampling frequency and referred to the Center of Gravity (CoG) of the car;
- an Occupant Restraint Controller (ORC) consisting in a 3 DoF IMU placed in the rear part of the car, measuring longitudinal and lateral acceleration as well as heading rate, the purpose is the airbag activation during a crash. The collected data are available with 100 Hz sampling frequency and referred to the vehicle CoG;
- four wheel encoders, sampled at 100 Hz, measuring the odometric velocity of each wheel;
- a steering angle sensor at the frontal wheels, sampled at 100 Hz.

In addition to on-board sensors, the vehicle is equipped with two further dedicated devices, specifically aimed at navigation. The first one is installed in the vehicle CoG, comprising a 6 DoF IMU plus a GNSS module from Suchy Data Systems GmbH [55]. The IMU extracts data at 100 Hz sampling frequency, while the GNSS module, working at 10 Hz sampling frequency, provides the latitude, longitude, geodetic altitude above sea level, planar velocity and heading of the vehicle. The second dedicated IMU+GNSS integrated sensor, from Inertial Sense [56], is rigidly mounted on top of the Scanbrick® radar (Fig. 7), aimed at providing a ground truth measurement of the radar 3D acceleration and 3D angular velocity. The IMU works at 250 Hz, while the GNSS at 2.5 Hz. In addition to the raw GNSS and IMU data, the radar co-located platform integrates a magnetometer, a barometer and provides the sensor position, velocity and orientation at the same IMU rate as output of a proprietary 3D INS tracking filter.

Finally, a 360 deg video camera has been placed on the vehicle rooftop to cross-check the acquired radar and navigation data.

The acquisition campaign was carried over a two-day period. Radar and navigation data were collected in various environments, mostly on a closed road in front of the Dipartimento di Elettronica, Informazione e Bioingegneria (DEIB) of Politecnico di Milano (Fig. 8) and on an open road around DEIB. Different vehicle trajectories were tested, in order to

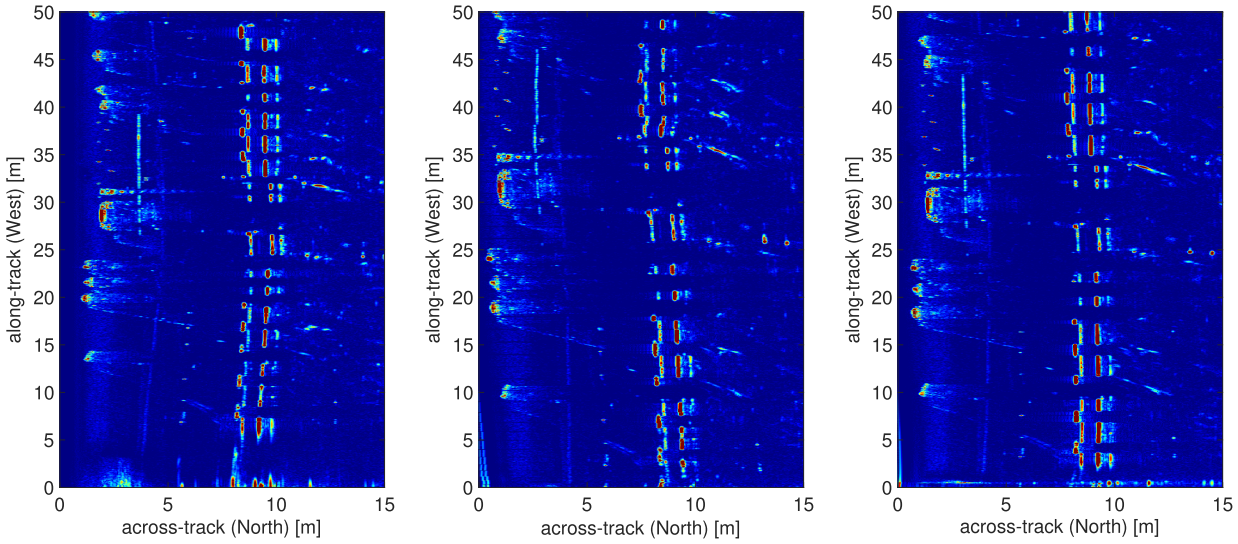

(a) No navigation (b) Commercial INS (IMU+GNSS) (c) Proposed SAR-MIN (on-board sensors)

FIGURE 10. SAR images of Test 1 obtained with different levels of navigation knowledge: (10a) without any navigation input; (10b) with commercial INS navigation data from dedicated IMU+GNSS platform; (10c) with SAR-MIN data from multiple on-board sensors (images not in scale).

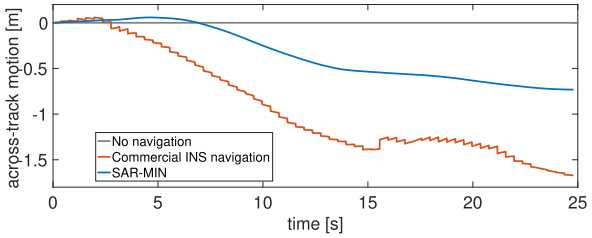

FIGURE 11. Comparison between the across-track motion estimated by commercial INS (red) and by the proposed SAR-MIN (blue) for Test 1.

TABLE 3. Data and image parameters used in SAR processing.

Parameter	Value(s)
Number of processed channels	8
Synthetic Aperture	variable (up to 1 m)
Pixel size in focused SAR images	4x4 cm
Range resolution	5 cm
Cross-range resolution	4 cm
Pointing angle of the processed beam	90 deg

analyze the effect of a non-straight motion, with curves and non-uniform travelling speed, on SAR imaging. A wide selection of targets was available, such as cars, bikes, motorbikes, building, people, trees, fences, lamp poles, etc, as well as artificial targets (corners) purposely placed along the observed scene.

V. RESULTS

We report the results concerning three selected trajectories of the experimental campaign, hereafter referred as Test 1, Test 2 and Test 3 respectively, ranging in length from 50 to 120 meters, where the maximum allowed speed is limited to approximately 20 km/h, given the PRF and the number of channels of the Scanbrick® platform. As an example, the GNSS-measured speed for Test 1 is reported in Fig. 9. For each trajectory, the radar data are processed using the TDBP algorithm described in Section III, taking as input the instantaneous position, velocity and orientation estimated with the tracking filters in Section II. In particular, SAR focusing is implemented by setting the weighting function $W(\cdot)$ in (23) so as to form SAR images at 90 deg with respect to the direction of motion, for a side-looking SAR. The same weighting function is also used to let the synthetic aperture A_s^{strip} vary depending on the distance from the radar sensor (up to 1 m at $R_{\max} = 27$ m), in such a way to achieve a quasi-constant linear resolution of 5 cm everywhere in the SAR image. Other relevant parameters are reported in Table 3.

A. TEST 1

The first result, in Fig. 10, 11 and 12, is related to the imaging of the side-scenario of Test 1, where the vehicle travels on an approximately straight trajectory of 50 m length (along-track motion), from East to West, slowly turning to the left (across-track motion). The three SAR images shown in Fig. 10 are obtained, respectively: (10a) without any navigation input and assuming a linear trajectory with constant speed; (10b) by employing a standard IMU+GNSS integrated navigation, i.e., the output of the commercial INS tracking filter of the dedicated on-radar sensor; (10c) the proposed SAR-MIN method in Subection II-B. The three images have the same

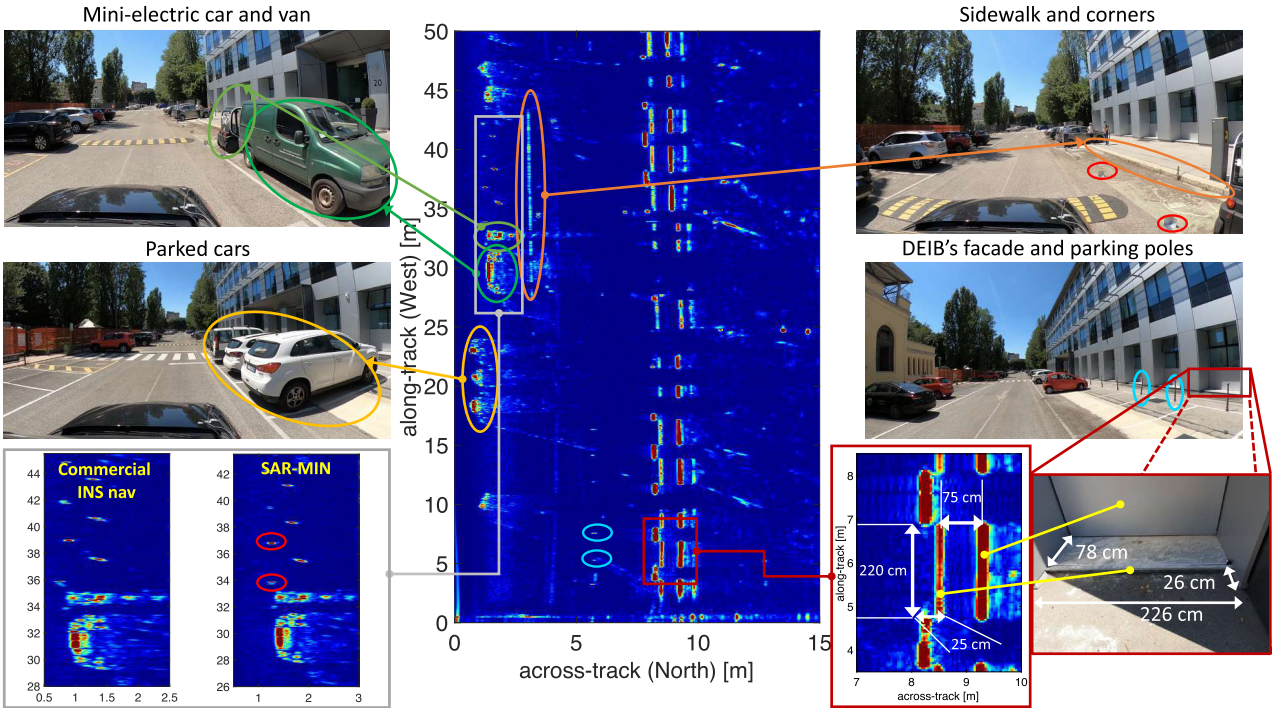

FIGURE 12. Test 1 targets from SAR imaging: with a SAR ad-hoc navigation over the trajectory, the targets in the scene appear bright and well focused. In particular, Test 1 allows to clearly identify the sidewalk (orange circle), artificial corners (red circles), parked cars (green and yellow circles) and the DEIB's facade, whose distinctive elements looks of the correct shape and dimensions (grey box, bottom right). The image detail (grey box, bottom left) allows to observe the focusing improvement on the van compared to the case of a non-specific navigation.

color scale. It can be noticed that, in the first two cases, localization is not accurate enough to enable high-resolution SAR focusing, as the imaging cannot be used to draw a precise description of the surrounding. By looking at the available targets, portrayed in detail in Fig. 12, we can take as reference the DEIB facade, constituted by alternated elements of known shape and dimensions, to evaluate the quality of the scene reconstruction. In Fig. 10a (no navigation), the facade appears as deformed and slightly stretched, as a consequence of position and velocity errors, respectively. This is easily noticed by observing that the facade is not straight as it should be, but instead follows the lateral motion (i.e., across-track motion) of the vehicle, which is about 50 cm over the full trajectory, the latter value being cross-checked against range-compressed radar data, not reported here. With the commercial INS (Fig. 10b), the overall imaging is slightly better, but still not well focused, due to the sawtooth-like trend of the estimated position from IMU and GNSS data, highlighted in Fig. 11 (red curve). These abrupt changes in the position estimate, which can range up to several cm, are due to the periodic GNSS corrections on the diverging IMU estimates, affected by residual uncompensated bias. As explained in Section II-A, the tracking filter model of the commercial INS is particularly sensitive to IMU biases [40], and the overall effect is to produce unwanted phase jumps negatively affecting the SAR focusing. Moreover, Fig. 11 shows how inaccurate navigation data of commercial INS overestimate the across-track vehicle motion leading to image deformation. Conversely, by fusing information from multiple sensors as in SAR-MIN, the quality of the image improves thus allowing to clearly retrieve the targets' shape and dimensions, as well as the vehicle-to-target distances. From Fig. 12, we can notice how the various targets in the scene appear in Fig. 10c: parked cars, a van and a mini-electric car, artificially placed reflective corners, 15 meters of sidewalk and the whole DEIB facade. In particular, the sidewalk clearly appears as perfectly straight in the image (to be compared with the same in Fig. 10b) and a direct comparison against hand-measurements of characteristic elements in the DEIB facade (at the bottom right of Fig. 12) allows to assess that SAR products can localize targets with a centimeter-level accuracy. In addition, it can be appreciated the relevant improvement in the image focusing by comparing the two image details of the van, the mini-electric car and the artificial corners, obtained with SAR-MIN and commercial navigation. We remark that the SAR performance improvement provided by SAR-MIN method is due to a fine-tuning of the SAR-MIN tracking filter (Section II-B), which integrates multiple heterogeneous sensors, and to a careful choice of the motion model, which must be selected according to the experienced dynamics.

B. TEST 2

The second result, concerning Test 2, is conceptually similar to the first one: we selected a 120 m long trajectory from West to East characterized by a double curve of approximately

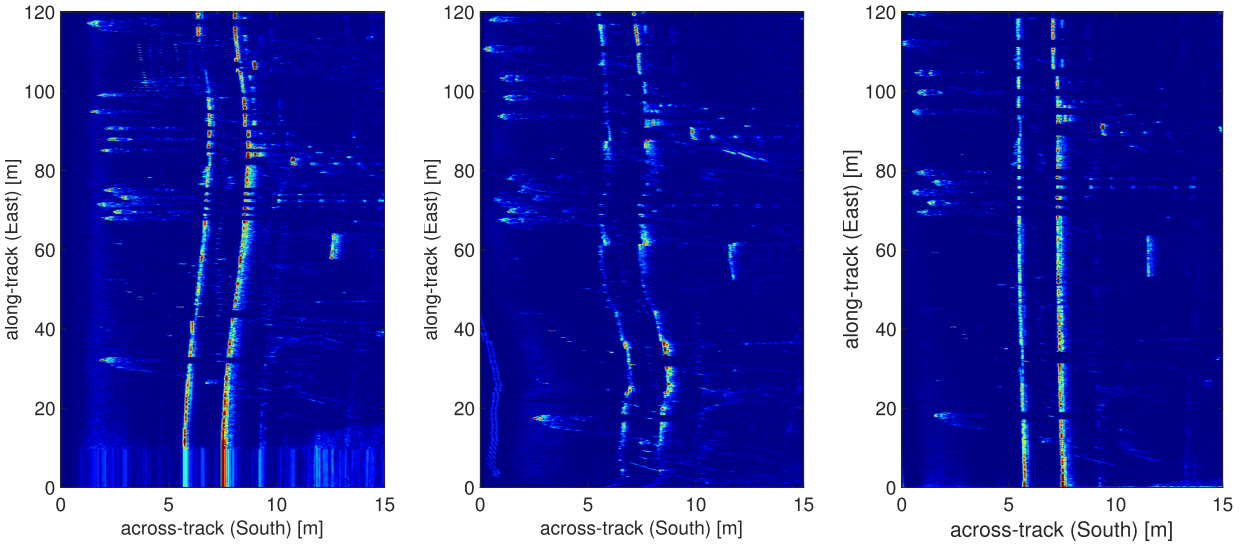

(a) No navigation (b) Commercial INS (IMU+GNSS) (c) Proposed SAR-MIN (on-board sensors)

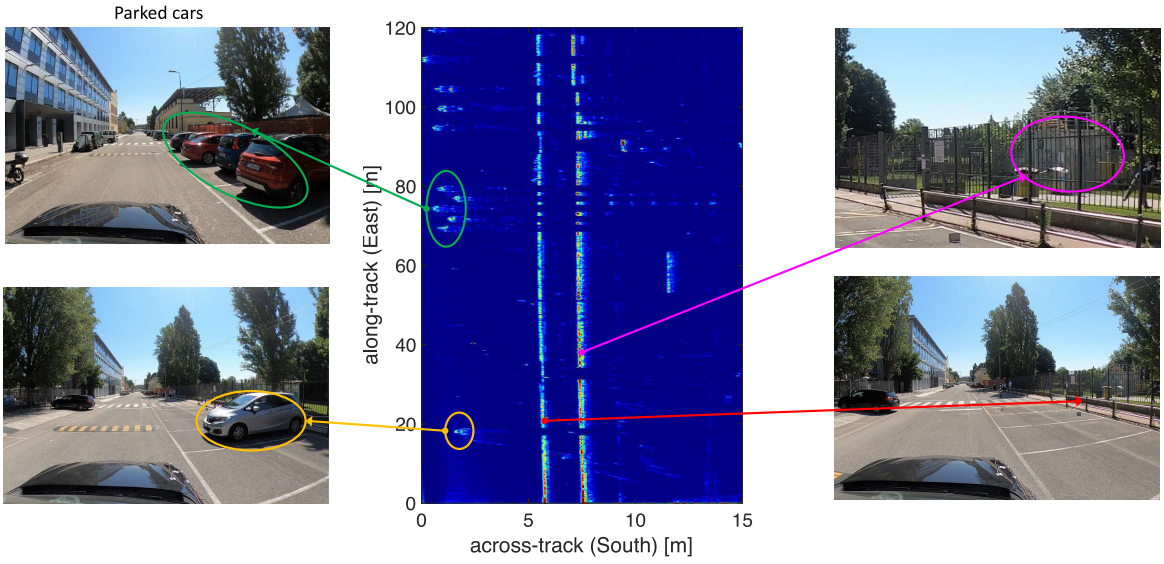

(d) Targets

FIGURE 13. Comparison among different SAR images of Test 2 (13a,13b,13c) and targets (13d). The first three images are organized as in Fig. 10, while the targets in the scene, especially the railing and the fence are correctly imaged.

±1 m cross-track (North-South). In this case, among the targets, parked cars, a railing and a fence, the latter two used as reference to assess the accuracy of navigation data in place of the DEIB facade. Figs. 13a, 13b and 13c report the same comparison made for Test 1 (Fig. 10), while Fig. 13d shows the Test 2 targets. The improvement on the quality of the SAR image provided by the proposed SAR-MIN method is equally evident as for Test 1, especially for the railing and the fence that appear well focused and straight as they should be, as can be noticed from Fig. 13d. In this case of motion affected by slow winding, the commercial navigation provides an even worse result than in Test 1, as shown in Fig. 14, reporting the estimated across-track motion for commercial INS (red curve) and SAR-MIN (blue curve).

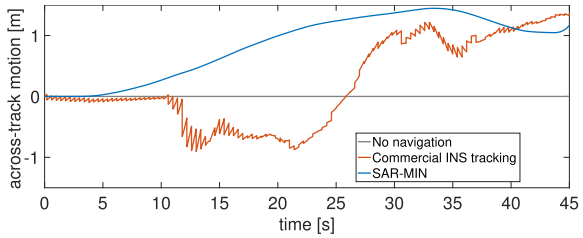

FIGURE 14. Comparison between the across-track motion estimated by commercial INS (red) and by the proposed SAR-MIN (blue) for Test 2.

C. TEST 3

The last results are related to a challenging track, performed in Test 3, where the vehicle travels from East to West on a zig-zag trajectory with moderate velocity.

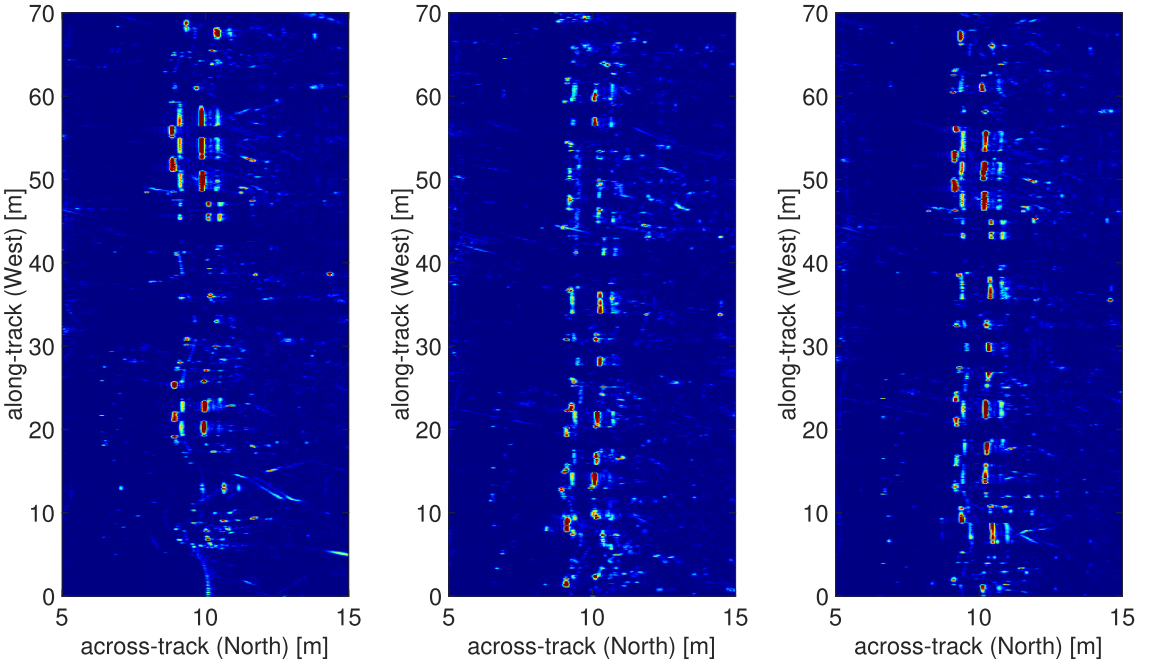

(a) No navigation (b) Commercial INS (IMU+GNSS) (c) Proposed SAR-MIN (on-board sensors)

FIGURE 15. Comparison among different SAR images of Test 3 (15a, 15b, 15c). The best overall reconstruction is still from ad-hoc processing of on-board sensors.

Fig. 15 reports the three SAR images of the DEIB facade, organized as in Figs. 10 and 13, i.e., without any navigation (15a), with commercial INS (15b) and with the proposed SAR-MIN method (15c). Once again, the proposed multi-sensor radar navigation provides a better imaging result compared to a standard, commercial solution: the overall best representation of the DEIB facade is in Fig. 15c, with better focused (brighter) elements, although not perfectly straight. Indeed, compared to Tests 1 and 2, the image is here affected by residual motion errors of various nature, mainly due to the limited accuracy of on-board sensors. Therefore, if on one hand this result encourages the improvement of the multi-sensor navigation, on the other hand it calls for the use of residual motion corrections based on joint processing of navigation *and* radar data, to accomplish meaningful environmental maps in all the possible travelling scenarios.

It is important to notice that the reconstructed trajectory with on-board sensors (SAR-MIN) is substantially equivalent to the one obtained with the same ad-hoc processing, but applied to the IMU and GNSS data of the dedicated sensor installed on the radar, apart from a 20 cm difference over the whole length (Fig. 16). This similarity has been observed on all the campaign trajectories, with difference ranging from a few centimeters to tens of centimeters. This suggests that, for urban tracks with medium-to-low dynamics, the dedicated on-radar sensor does not add any information compared to the measurements of on-baord sensors, confirming the validity

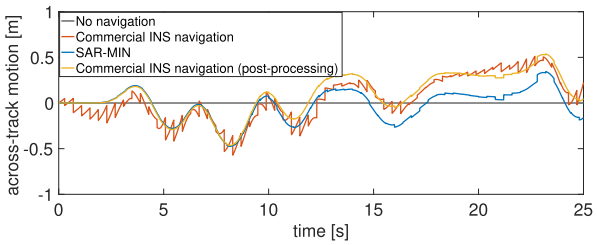

FIGURE 16. Comparison between estimated across-track motions in Test 3: the SAR-MIN method (blue) attains similar performance to a dedicated post-processing of IMU and GNSS data from the commercial on-radar sensor, used as benchmark (yellow).

of the proposed SAR-MIN approach that does not require SAR-dedicated sensors but rather aims at improving the processing of available data.

VI. CONCLUSION AND OPEN CHALLENGES

This paper proposes and validates by experimental tests a SAR system for mapping the driving environment in automotive applications. A key component is the ad-hoc navigation processing algorithm that accesses the internal vehicle data-bus to integrate heterogeneous on-board sensors to extract accurate location information and enable high-resolution SAR imaging. The results clearly demonstrate the ability of the navigation-assisted SAR system to build accurate maps of the driving environment, with much finer resolution than allowed by current high-end automotive radars. For scenarios with moderate dynamics, SAR

processing can effectively leverage only on navigation data to obtain high-quality, meaningful images with a centimeter-level resolution. The use of dedicated, commercial on-radar navigation sensors in not enough, in general, to achieve the same performance, unless a specific post-processing is applied. The following challenges are expected to be addressed by future researches, listed in the following.

Assessment in higher-dynamic road conditions. Extensive experimental campaigns are needed to investigate the performance of the proposed navigation-imaging system in challenging vehicular scenarios with rough roads, high velocities or urban canyons with poor GNSS coverage. Tracking algorithms must provide seamless accurate navigation over long time scales, which might require changing the implementation. From the hardware point of view, extending SAR imaging to high velocities implies an increase in the required PRF or the number of virtual radar channels. In this regard, it is helpful assessing the quality of SAR images by relaxing the requirements on the PRF, considering a trade-off between transmitted PRF, imaging quality, and number of virtual channels. Of course, the use of cost-effective sensors is one of the key-enablers of mass-market automotive SAR products.

Residual motion correction. Residual motion errors result in uncompensated phase terms that affect imaging quality. The results highlighted that navigation data from automotive sensors can be affected by cm-scale drifts and residual inaccuracies, especially on challenging tracks, causing mispositioning and defocusing. This issue can be tackled by developing a residual motion compensation method based on the joint processing of navigation and radar data, tailoring the strategy to automotive applications.

Computational burden. The computational burden of the TDBP used in this paper is not yet suited for real-time applications. As discussed in Section III-C, an efficient SAR processing algorithm must be designed with a trade-off between the quality of the focusing and the complexity, towards the goal of real-time implementation. TDBP is a highly-parallelizable algorithm, for which efficient implementations exist either based on processing scheme – like Fast-factorized BP (FFBP) [57] – or Graphical Processing Units (GPU) [44]. The alternative to TDBP is represented by focusing algorithms based on specific assumptions on platform motion, such as Chirp-Scaling or Omega-K [58], [59]. Such algorithms are well known to provide high-quality imaging in the case of uniform motion, but result in degraded performance in the case of strongly non-linear trajectories. At this stage of the research, we deem it is still debatable whether the optimal solution for automotive SAR should include efficient, and possibly GPU-based, TDBP processing, or rather SAR focusing algorithms based on specific assumptions on vehicle motion, letting this point open for further research. Moreover, we also deem future researches on automotive SAR processing should consider the role of ghost targets arising from either imaging ambiguities or multipath phenomena [27], [60].

Extension to 3D SAR imaging. Although not investigated in this work, SAR can provide 3D images of the surrounding, focusing targets on the elevation plane. Of course, the navigation must be generalized from 2D to 3D and also SAR processing becomes more computational demanding. In this regard, dedicated experimental activities are needed to investigate the real benefits of 3D SAR imaging in realistic automotive scenarios.

ACKNOWLEDGMENT

The research has been carried out in the framework of the Huawei-Politecnico di Milano Joint Research Lab on automotive SAR. The authors would like to acknowledge Huawei Münich Research Center, Huawei Milan Research Center and Huawei Wireless BU, and Dr. Paolo Falcone from ARESYS S.r.l. for the cooperation and support in the data acquisition campaign. A grateful acknowledge to Prof. Sergio Savaresi for the provision of the Alfa Romeo car.

REFERENCES

[1] *Taxonomy and Definitions for Terms Related to on-Road Motor Vehicle Automated Driving Systems*, SAE International, Warrendale, PA, USA, Jan. 2014.
[2] E. Marti, M. A. de Miguel, F. Garcia, and J. Perez, "A review of sensor technologies for perception in automated driving," *IEEE Intell. Transp. Syst. Mag.*, vol. 11, no. 4, pp. 94–108, Sep. 2019.
[3] M. Brambilla, M. Nicoli, G. Soatti, and F. Deflorio, "Augmenting vehicle localization by cooperative sensing of the driving environment: Insight on data association in urban traffic scenarios," *IEEE Trans. Intell. Transp. Syst.*, vol. 21, no. 4, pp. 1646–1663, Apr. 2020.
[4] J. Hasch, E. Topak, R. Schnabel, T. Zwick, R. Weigel, and C. Waldschmidt, "Millimeter-wave technology for automotive radar sensors in the 77 GHz frequency band," *IEEE Trans. Microw. Theory Techn.*, vol. 60, no. 3, pp. 845–860, Mar. 2012.
[5] *System Reference Document (SRdoc); Transmission Characteristics; Technical Characteristics for Radiodetermination Equipment for Ground Based Vehicular Applications With in the Frequency Range 77 GHz to 81 GHz*, document ETSI TR 103 593 v.1.1.1, ETSI, 2020. [Online]. Available: https://www.etsi.org/deliver/etsi_tr/103500_103599/103593/01.01.01_60/tr_103593v010101p.pdf
[6] S. Brisken, F. Ruf, and F. Höhne, "Recent evolution of automotive imaging radar and its information content," *IET Radar, Sonar Navigat.*, vol. 12, no. 10, pp. 1078–1081, Oct. 2018.
[7] M. Schoen, M. Horn, M. Hahn, and J. Dickmann, "Real-time radar SLAM," in *Proc. 11th Workshop Fahrerassistenzsysteme Automatisiertes Fahren*. Uni-DAS e. V., 2017, pp. 1–11.
[8] H. Wu and T. Zwick, "Automotive SAR for parking lot detection," in *Proc. German Microw. Conf.*, Mar. 2009, pp. 1–8.
[9] H. Wu and T. Zwick, "A novel motion compensation algorithm for automotive SAR: Simulations and experiments," in *Proc. German Microw. Conf. Dig. Papers*, Mar. 2010, pp. 222–226.
[10] H. Iqbal, M. B. Sajjad, M. Mueller, and C. Waldschmidt, "SAR imaging in an automotive scenario," in *Proc. IEEE 15th Medit. Microw. Symp. (MMS)*, Nov. 2015, pp. 1–4.
[11] F. Harrer, F. Pfeiffer, A. Loffler, T. Gisder, and E. Biebl, "Synthetic aperture radar algorithm for a global amplitude map," in *Proc. 14th Workshop Positioning, Navigat. Commun. (WPNC)*, Oct. 2017, pp. 1–6.
[12] F. Ulaby and D. Long, *Microwave Radar and Radiometric Remote Sensing*. Norwood, MA, USA: Artech House, 2015. [Online]. Available: http://cds.cern.ch/record/2197387
[13] A. Moreira, P. Prats-Iraola, M. Younis, G. Krieger, I. Hajnsek, and K. P. Papathanassiou, "A tutorial on synthetic aperture radar," *IEEE Geosci. Remote Sens. Mag.*, vol. 1, no. 1, pp. 6–43, Mar. 2013.
[14] A. Ferretti, A. Monti-Guarnieri, C. Prati, F. Rocca, and D. Massonet, "InSAR principles—Guidelines for SAR interferometry processing and interpretation," *ESA Training Manual*, vol. 19, pp. 7–13, Jan. 2007. [Online]. Available: https://www.esa.int/esapub/tm/tm19/TM-19_ptA.pdf

[15] M. Mariotti D'Alessandro and S. Tebaldini, "Digital terrain model retrieval in tropical forests through P-Band SAR tomography," *IEEE Trans. Geosci. Remote Sens.*, vol. 57, no. 9, pp. 6774–6781, Sep. 2019.

[16] H. Wu, L. Zwirello, X. Li, L. Reichardt, and T. Zwick, "Motion compensation with one-axis gyroscope and two-axis accelerometer for automotive SAR," in *Proc. German Microw. Conf.*, Mar. 2011, pp. 1–4.

[17] R. Feger, A. Haderer, and A. Stelzer, "Experimental verification of a 77-GHz synthetic aperture radar system for automotive applications," in *IEEE MTT-S Int. Microw. Symp. Dig.*, Mar. 2017, pp. 111–114.

[18] A. Laribi, M. Hahn, J. Dickmann, and C. Waldschmidt, "Performance investigation of automotive SAR imaging," in *IEEE MTT-S Int. Microw. Symp. Dig.*, Apr. 2018, pp. 1–4.

[19] R. Wang, J. Pei, Y. Zhang, M. Li, Y. Huang, and J. Wu, "An auxiliary parking method based on automotive millimeter wave SAR," in *Proc. IEEE Int. Geosci. Remote Sens. Symp. IGARSS*, Jul. 2019, pp. 2503–2506.

[20] M. Caris, S. Stanko, S. Palm, R. Sommer, A. Wahlen, and N. Pohl, "300 GHz radar for high resolution SAR and ISAR applications," in *Proc. 16th Int. Radar Symp. (IRS)*, Jun. 2015, pp. 577–580.

[21] S. Stanko, S. Palm, R. Sommer, F. Kloppel, M. Caris, and N. Pohl, "Millimeter resolution SAR imaging of infrastructure in the lower THz region using MIRANDA-300," in *Proc. 46th Eur. Microw. Conf. (EuMC)*, Oct. 2016, pp. 358–361.

[22] H. Wu, "Motion compensation for near-range synthetic aperture radar applications," Ph.D. dissertation, Inst. Radio Freq. Eng. Electron., Karlsruhe Inst. Technol., Karlsruhe, Germany, 2012.

[23] T. A. Kennedy, "Strapdown inertial measurement units for motion compensation for synthetic aperture radars," *IEEE Aerosp. Electron. Syst. Mag.*, vol. 3, no. 10, pp. 32–35, Oct. 1988.

[24] D. Blacknell and S. Quegan, "SAR motion compensation using autofocus," *Int. J. Remote Sens.*, vol. 12, no. 2, pp. 253–275, Feb. 1991, doi: 10.1080/01431169108929651.

[25] J. Torgrimsson, P. Dammert, H. Hellsten, and L. M. H. Ulander, "SAR processing without a motion measurement system," *IEEE Trans. Geosci. Remote Sens.*, vol. 57, no. 2, pp. 1025–1039, Feb. 2019.

[26] S. Tebaldini, T. Nagler, H. Rott, and A. Heilig, "Imaging the internal structure of an alpine glacier via L-Band airborne SAR tomography," *IEEE Trans. Geosci. Remote Sens.*, vol. 54, no. 12, pp. 7197–7209, Dec. 2016.

[27] Y. Yu, M. M. d'Alessandro, S. Tebaldini, and M. Liao, "Signal processing options for high resolution SAR tomography of natural scenarios," *Remote Sens.*, vol. 12, no. 10, p. 1638, May 2020. [Online]. Available: https://www.mdpi.com/2072-4292/12/10/1638

[28] O. Frey, C. Magnard, M. Ruegg, and E. Meier, "Focusing of airborne synthetic aperture radar data from highly nonlinear flight tracks," *IEEE Trans. Geosci. Remote Sens.*, vol. 47, no. 6, pp. 1844–1858, Jun. 2009.

[29] O. Ponce, P. Prats-Iraola, M. Pinheiro, M. Rodriguez-Cassola, R. Scheiber, A. Reigber, and A. Moreira, "Fully polarimetric high-resolution 3-D imaging with circular SAR at L-band," *IEEE Trans. Geosci. Remote Sens.*, vol. 52, no. 6, pp. 3074–3090, Jun. 2014.

[30] S. Perna *et al.*, "The ASI integrated sounder-SAR system operating in the UHF-VHF bands: First results of the 2018 helicopter-borne morocco desert campaign," *Remote Sens.*, vol. 11, no. 16, p. 1845, Aug. 2019. [Online]. Available: https://www.mdpi.com/2072-4292/11/16/1845

[31] R. De Paulis, C. Prati, F. Rocca, S. Scirpoli, and S. Tebaldini, "Focusing synthetic aperture sonar (SAS) data with the Omega-K technique," in *Proc. IEEE Int. Geosci. Remote Sens. Symp.*, Jul. 2009, pp. I-68–I-71.

[32] R. De Paulis, C. Prati, S. Scirpoli, F. Rocca, A. Tesei, P. A. Sletner, S. Biagini, P. Guerrini, F. Gasparoni, C. Carmisciano, and M. Locritani, "SAS multipass interferometry for monitoring seabed deformation using a high-frequency imaging sonar," in *Proc. OCEANS IEEE Spain*, Jun. 2011, pp. 1–10.

[33] F. Fembacher, F. B. Khalid, G. Balazs, D. T. Nugraha, and A. Roger, "Real-time synthetic aperture radar for automotive embedded systems," in *Proc. 15th Eur. Radar Conf. (EuRAD)*, Sep. 2018, pp. 517–520.

[34] T. Kan, G. Xin, L. Xiaowei, and L. Zhongshan, "Implementation of real-time automotive SAR imaging," in *Proc. IEEE 11th Sensor Array Multichannel Signal Process. Workshop (SAM)*, Jun. 2020, pp. 1–4.

[35] T. Gisder, M.-M. Meinecke, and E. Biebl, "Synthetic aperture radar towards automotive applications," in *Proc. 20th Int. Radar Symp. (IRS)*, Jun. 2019, pp. 1–10.

[36] *Compact Dual Antenna SPAN Enclosure Delivers 3D Position, Velocity Attitude*, NovAtel Inc., Calgary, AB, Canada, 2018.

[37] F. Zhang, H. Stahle, G. Chen, C. C. C. Simon, C. Buckl, and A. Knoll, "A sensor fusion approach for localization with cumulative error elimination," in *Proc. IEEE Int. Conf. Multisensor Fusion Integr. Intell. Syst. (MFI)*, Sep. 2012, pp. 1–6.

[38] S. Kuutti, S. Fallah, K. Katsaros, M. Dianati, F. Mccullough, and A. Mouzakitis, "A survey of the state-of-the-art localization techniques and their potentials for autonomous vehicle applications," *IEEE Internet Things J.*, vol. 5, no. 2, pp. 829–846, Apr. 2018.

[39] M. Brambilla, L. Combi, A. Matera, D. Tagliaferri, M. Nicoli, and U. Spagnolini, "Sensor-aided V2X beam tracking for connected automated driving: Distributed architecture and processing algorithms," *Sensors*, vol. 20, no. 12, p. 3573, Jun. 2020.

[40] M. Kok, J. D. Hol, and T. B. Schön, "Using inertial sensors for position and orientation estimation," *Found. Trends Signal Process.*, vol. 11, nos. 1–2, pp. 1–153, 2017.

[41] P. D. Groves, "Principles of GNSS, inertial, and multisensor integrated navigation systems, 2nd edition [book review]," *IEEE Aerosp. Electron. Syst. Mag.*, vol. 30, no. 2, pp. 26–27, Feb. 2015.

[42] G. Wan, X. Yang, R. Cai, H. Li, Y. Zhou, H. Wang, and S. Song, "Robust and precise vehicle localization based on multi-sensor fusion in diverse city scenes," in *Proc. IEEE Int. Conf. Robot. Autom. (ICRA)*, May 2018, pp. 4670–4677.

[43] M. Steiner, T. Grebner, and C. Waldschmidt, "Millimeter-wave SAR-imaging with radar networks based on radar self-localization," *IEEE Trans. Microw. Theory Techn.*, vol. 68, no. 11, pp. 4652–4661, Nov. 2020.

[44] T. Gisder, F. Harrer, and E. Biebl, "Application of a stream-based SAR-backprojection approach for automotive environment perception," in *Proc. 19th Int. Radar Symp. (IRS)*, Jun. 2018, pp. 1–10.

[45] M. I. Duersch and D. G. Long, "Analysis of time-domain back-projection for stripmap SAR," *Int. J. Remote Sens.*, vol. 36, no. 8, pp. 2010–2036, Apr. 2015.

[46] V. M. N. Passaro, A. Cuccovillo, L. Vaiani, M. De Carlo, and C. E. Campanella, "Gyroscope technology and applications: A review in the industrial perspective," *Sensors*, vol. 17, no. 10, p. 2284, Oct. 2017.

[47] R. Gonzalez and P. Dabove, "Performance assessment of an ultra low-cost inertial measurement unit for ground vehicle navigation," *Sensors*, vol. 19, no. 18, p. 3865, Sep. 2019.

[48] N. El-Sheimy and A. Youssef, "Inertial sensors technologies for navigation applications: State of the art and future trends," *Satell. Navigat.*, vol. 1, no. 1, pp. 1–21, Dec. 2020.

[49] R. Schubert, E. Richter, and G. Wanielik, "Comparison and evaluation of advanced motion models for vehicle tracking," in *Proc. 11th Int. Conf. Inf. Fusion*, Jun. 2008, pp. 1–6.

[50] H. Heisler, *Advanced Vehicle Technology*. London, U.K.: Hodder and Stoughton, 1989.

[51] E. A. Wan and R. Van Der Merwe, "The unscented Kalman filter for nonlinear estimation," in *Proc. IEEE Adapt. Syst. Signal Process., Commun., Control Symp.*, Oct. 2000, pp. 153–158.

[52] E. C. Zaugg and D. G. Long, "Generalized frequency scaling and back-projection for LFM-CW SAR processing," *IEEE Trans. Geosci. Remote Sens.*, vol. 53, no. 7, pp. 3600–3614, Jul. 2015.

[53] F. Harrer, F. Pfeiffer, A. Loffler, T. Gisder, C. Buchberger, and E. Biebl, "Multi channel approaches for an automotive synthetic aperture radar," in *Proc. 11th German Microw. Conf. (GeMiC)*, Mar. 2018, pp. 391–394.

[54] P. Guccione, A. M. Guarnieri, F. Rocca, D. Giudici, and N. Gebert, "Along-track multistatic synthetic aperture radar formations of minisatellites," *Remote Sens.*, vol. 12, no. 1, p. 124, 2020. [Online]. Available: https://www.mdpi.com/2072-4292/12/1/124

[55] *xProGPS Nano Operating Manual*, Suchy Data Systems GmbH, Erdweg, Germany, 2019.

[56] *uIMU, uAHRS, uINS+RTK, uINS-Dual Calibrated Inertial Systems With Onboard GPS*, Inertial Sense, Lindon, UT, USA, 2020.

[57] L. M. H. Ulander, H. Hellsten, and G. Stenstrom, "Synthetic-aperture radar processing using fast factorized back-projection," *IEEE Trans. Aerosp. Electron. Syst.*, vol. 39, no. 3, pp. 760–776, Jul. 2003.

[58] A. Moreira, J. Mittermayer, and R. Scheiber, "Extended chirp scaling algorithm for air- and spaceborne SAR data processing in stripmap and ScanSAR imaging modes," *IEEE Trans. Geosci. Remote Sens.*, vol. 34, no. 5, pp. 1123–1136, Sep. 1996.

[59] C. Cafforio, C. Prati, and F. Rocca, "SAR data focusing using seismic migration techniques," *IEEE Trans. Aerosp. Electron. Syst.*, vol. 27, no. 2, pp. 194–207, Mar. 1991.

[60] C. Liu, S. Liu, C. Zhang, Y. Huang, and H. Wang, "Multipath propagation analysis and ghost target removal for FMCW automotive radars," in *Proc. IET Int. Radar Conf.(IRC)*, Nov. 2020, pp. 1–5.

DARIO TAGLIAFERRI (Member, IEEE) received the B.Sc., M.Sc., and Ph.D. degrees in telecommunication engineering from the Politecnico di Milano, Italy, in 2012, 2015, and 2019, respectively. He is currently a Postdoctoral Research Fellow with the Dipartimento di Elettronica, Informazione e Bioingegneria, Politecnico di Milano, in the framework of Huawei-Polimi Joint Research Lab. His research interests comprise signal processing techniques for navigation and wireless communication systems, in particular, for sensor fusion of on-board sensors and MIMO channel estimation in 5G systems and beyond.

MARCO RIZZI (Graduate Student Member, IEEE) received the M.S. degree in telecommunication engineering from the Politecnico di Milano, Milan, Italy, in 2019. He is currently pursuing the Ph.D. degree in information technology with the Remote Sensing Group, Politecnico di Milano. From November 2019 to November 2020, he was a Research Fellow with the Politecnico di Milano, where he was involved in the research of optimal signal processing for automotive synthetic aperture radar (SAR). His main research interest is SAR signal processing, with an emphasis on image formation for distributed SAR systems.

MONICA NICOLI (Member, IEEE) received the M.Sc. degree *(cum laude)* in telecommunication engineering and the Ph.D. degree in electronic and communication engineering from the Politecnico di Milano, Milan, Italy, in 1998 and 2002, respectively. She was a Visiting Researcher with ENI-Agip, Italy, from 1998 to 1999, and also with Uppsala University, Sweden, in 2001. In 2002, she joined the Politecnico di Milano as a Faculty Member. She is currently an Associate Professor of Telecommunications with the Department of Management, Economics and Industrial Engineering, Politecnico di Milano, where she teaches localization, navigation and smart mobility and communication technologies for vehicles. Her research interests cover wireless communications and signal processing for ITS, with an emphasis on V2X communications, localization and navigation, cooperative and distributed systems for the Internet of Vehicles. She has coauthored 120 scientific publications (journals, conferences, and patents). She is a recipient of the Marisa Bellisario Award (1999), and a co-recipient of the Best Paper Awards of the IEEE Statistical Signal Processing Workshop (2018) and the IET Intelligent Transport Systems Journal (2014). She has served as an Associate Editor of the *EURASIP Journal on Wireless Communications and Networking* from 2010 to 2017, and as a Lead Guest Editor for the Special Issue on Localization in Mobile Wireless and Sensor Networks in 2011.

STEFANO TEBALDINI (Senior Member, IEEE) received the M.S. degree in telecommunication engineering and the Ph.D. degree from the Politecnico di Milano, in 2005 and 2009, respectively. Since 2005, he has been with the Digital Signal Processing Research Group, Politecnico di Milano, where he currently holds the position of Associate Professor. His research activities mostly focus on Earth Observation with Synthetic Aperture Radar (SAR) and Radar design and processing. He is one of the inventors of a new technology patented by T.R.E. for the exploitation of multiple interferograms in presence of distributed scattering. He teaches courses on signal theory and remote sensing at the Politecnico di Milano. He has been involved as a key scientist in several studies by the European Space Agency (ESA) concerning the tomographic phase of BIOMASS. He was a member of the SAOCOM-CS ESA Expert Group and is currently a member of the BIOMASS MAG at ESA.

IVAN RUSSO (Senior Member, IEEE) was born in Vibo Valentia, Italy, in 1982. He received the B.Sc. degree in electronics engineering and the M.Sc. degree in telecommunications engineering from the University of Calabria, Rende, Italy, in 2003 and 2007, respectively, and the Ph.D. degree in electronics engineering from the Mediterranean University of Reggio Calabria, Reggio Calabria, Italy, in 2011, with a focus on quasi-optical (QO) amplifiers, active FSSs, and efficient array beamforming networks. From 2010 to 2011, he was with the Department of Microwave Technology, University of Ulm, Ulm, Germany, where he was involved in high-resolution near-field probes and characterization of overmoded waveguides. From 2011 to 2013, he was a University Assistant with the Institute for Microwave and Photonics Engineering, TU Graz, Graz, Austria, where he was involved in spherical near/far-field transformations, RFID antennas, and circularly and dual-polarized UWB antennas. From 2013 to 2014, he was an EMC/Antenna Engineer with Thales Alenia Space, Turin, Italy, where he was involved in installed antenna performance on satellites. From 2014 to 2018, he was an Antenna Engineer with Elettronica S.p.A., Rome, Italy, where he focused on the development of UWB antennas and phased arrays for electronic warfare applications. Since 2018, he has been with the Huawei Research Center, Milan, Italy, as an Antenna and Phased Array Engineer, where he is currently focusing on innovative automotive radar antennas and systems and advanced solution for phased arrays and high-speed interconnects.

ANDREA VIRGILIO MONTI-GUARNIERI (Senior Member, IEEE) received the M.Sc. degree *(cum laude* in electronic engineering, in 1988. He has been a Full Professor with the Dipartimento di Elettronica, Informazione e Bioingegneria, since 2017. He is the Founder of Polimi spin-off Aresys (2003), targeting SAR, radar, and geophysics applications. He has an H index (Google) of 33, 5400 citations, received four conference awards, and holds applications for five patents. His current research interests focus on radar-based system design, calibration, MIMO, and geosynchronous SAR. He has been a reviewer of several scientific journals, Guest Editor for *MPI Remote Sensing*, and a member in scientific-technical committees of international workshops and symposia on Radar and Earth Observation (EO).

CLAUDIO MARIA PRATI is currently a Full Professor of Telecommunications with the Electronic Department, Politecnico of Milano (POLIMI). He has chaired the Telecommunications Study Council at POLIMI. He holds five patents in the field of SAR and SAS data processing. He has been awarded three prizes from the IEEE Geoscience and Remote Sensing Society (IGARSSâĂŹ89 and IGARSSâĂŹ99 and best TGARSS paper 2016). He has published more than 150 papers on SAR and SAS data processing and Interferometry. He has been involved as the key scientist in several studies by the European Space Agency (ESA), the European Union (EU), the Italian National Research Council (CNR), the Italian Space Agency (ASI), and ENI-AGIP. He is the Co-Founder of Tele-Rilevamento Europa (T.R.E), a spin-off company of POLIMI that has recently become T.R.E Altamira, a CLS French group company.

UMBERTO SPAGNOLINI (Senior Member, IEEE) is currently a Professor of Statistical Signal Processing, the Director of Joint Lab Huawei-Politecnico di Milano, and Huawei Industry Chair. His research in statistical signal processing covers remote sensing and communication systems with more than 300 papers on peer-reviewed journals/conferences and patents. He is the author of the book *Statistical Signal Processing in Engineering* (J. Wiley, 2017). His specific areas of interest include mmW channel estimation and space-time processing for single/multi-user wireless communication systems, cooperative and distributed inference methods including V2X systems, mmWave communication systems, parameter estimation/tracking, focusing and wavefield interpolation for remote sensing (UWB radar and oil exploration). He was a recipient/co-recipient of Best Paper Awards on geophysical signal processing methods (from EAGE), array processing (ICASSP 2006), and distributed synchronization for wireless sensor networks (SPAWC 2007, WRECOM 2007). He is a Technical Expert of standard-essential patents and IP. He has served as a part of the IEEE Editorial boards as well as a member in technical program committees of several conferences for all the areas of interests.